

# Catalysis Science & Technology

Accepted Manuscript



This article can be cited before page numbers have been issued, to do this please use: R. Zhong, Z. Zhang, S. Luo, Z. C. Zhang, L. Huang and M. Gu, *Catal. Sci. Technol.*, 2018, DOI: 10.1039/C8CY00965A.



This is an Accepted Manuscript, which has been through the Royal Society of Chemistry peer review process and has been accepted for publication.

Accepted Manuscripts are published online shortly after acceptance, before technical editing, formatting and proof reading. Using this free service, authors can make their results available to the community, in citable form, before we publish the edited article. We will replace this Accepted Manuscript with the edited and formatted Advance Article as soon as it is available.

You can find more information about Accepted Manuscripts in the [author guidelines](#).

Please note that technical editing may introduce minor changes to the text and/or graphics, which may alter content. The journal's standard [Terms & Conditions](#) and the ethical guidelines, outlined in our [author and reviewer resource centre](#), still apply. In no event shall the Royal Society of Chemistry be held responsible for any errors or omissions in this Accepted Manuscript or any consequences arising from the use of any information it contains.



## Journal Name

## ARTICLE

# Comparison of TiO<sub>2</sub> and g-C<sub>3</sub>N<sub>4</sub> 2D/2D nanocomposites from three synthesis protocols for visible-light induced hydrogen evolution

Received 00th January 20xx,  
Accepted 00th January 20xx

DOI: 10.1039/x0xx00000x

www.rsc.org/

Ruyi Zhong,<sup>a,b</sup> Zisheng Zhang,<sup>a</sup> Shuqi Luo,<sup>a</sup> Z. Conrad Zhang,<sup>b</sup> Limin Huang,<sup>a,\*</sup> and Meng Gu<sup>c,\*</sup>

Knowledge of the interfacial structure of nanocomposite materials is a prerequisite for rational design of nanostructured photocatalysts. Herein, TiO<sub>2</sub> and g-C<sub>3</sub>N<sub>4</sub> 2D/2D nanocomposites were fabricated from three distinct synthetic protocols (*i.e.*, co-calcination, solvothermal treatment and charge-induced aggregation), showing different degrees of enhancement (1.4–6.1 folds) in the visible-light induced photocatalytic hydrogen evolution reaction compared to the simple physical mixture. We propose that interfacial Ti–O–N covalent bonding promotes the charge carrier transfer and separation more effectively than the electrostatic interaction, thus accelerating photocatalytic H<sub>2</sub> production. Meanwhile, the exposed surface area of TiO<sub>2</sub> in the composite needs to be enlarged for deposition of co-catalyst. This research sheds light on the rational design of hybrid nanocomposites based on earth-abundant elements for photocatalysis.

## Introduction

Hydrogen is a promising clean energy carrier, as an environmentally friendly alternative to conventional fossil fuels, owing to its high combustion energy and zero emission.<sup>1–3</sup> Photocatalytic water splitting using solar energy by semiconductor photocatalysts has received intensive research interest in recent decades.<sup>4,5</sup> Fujishima and Honda originally proposed non-toxic TiO<sub>2</sub> as a stable benchmark photocatalyst under UV irradiation.<sup>6</sup> However, the large bandgap of TiO<sub>2</sub> (*ca.* 3.2 eV) restricts its utilization of the whole solar spectrum, as UV light accounts for only 4% proportion and visible light (400–800 nm) is dominating (50%). Doping TiO<sub>2</sub> with various elements or self-doping with Ti<sup>3+</sup> could extend its optical absorption to the visible-light range, however, usually suffers from the rapid photogenerated electron-hole recombination and the reduced stability of the doped materials.<sup>7,8</sup>

Recently, g-C<sub>3</sub>N<sub>4</sub> has been identified as a promising organic semiconductor for photocatalytic applications, including photoreduction of H<sub>2</sub>O to H<sub>2</sub>.<sup>5,9–14</sup> Bulk g-C<sub>3</sub>N<sub>4</sub> prepared from

facile pyrolysis of nitrogen-rich precursors has a suitable band structure with a low band gap of *ca.* 2.7 eV to harvest visible light, but its photocatalytic performance is limited by the low surface area and fast recombination rate of photogenerated charge carriers.<sup>12–17</sup> Exfoliation of g-C<sub>3</sub>N<sub>4</sub> to 2D nanosheets by various chemical and physical approaches could increase surface area and reduce charge recombination, but the problem of re-stacking remains.<sup>9,10,12,13</sup>

Constructing heterojunction structures of TiO<sub>2</sub> and g-C<sub>3</sub>N<sub>4</sub> have been proven as a cost-effective way to avoid the above drawbacks of each component and realize a synergic effect in promoting the efficient generation and separation of charge carriers, and thus boosting the photocatalytic activity.<sup>12,18,19</sup> The heterostructure interfaces would offer a premise for such synergism during photocatalytic reactions by forming different types of band diagrams.<sup>12,18,19</sup> Therefore many efforts have been made to fabricate TiO<sub>2</sub> with g-C<sub>3</sub>N<sub>4</sub> to form a composite with abundant heterostructure interfaces. Most of the fabrications of heterostructures are based on simultaneous formation of heterojunctions and one (or both) of the components.<sup>20–31</sup> For instance, solvothermal synthesis of nanostructured TiO<sub>2</sub> have been performed in the presence of the pre-synthesized bulk g-C<sub>3</sub>N<sub>4</sub>,<sup>20</sup> thermal exfoliated g-C<sub>3</sub>N<sub>4</sub>,<sup>22,23</sup> oxidized g-C<sub>3</sub>N<sub>4</sub>,<sup>21,24</sup> or protonated g-C<sub>3</sub>N<sub>4</sub>,<sup>25</sup> forming particles attached on sheets,<sup>20–23</sup> or nanosheets to nanosheets assembly<sup>24,25</sup>, outperforming bare TiO<sub>2</sub> or g-C<sub>3</sub>N<sub>4</sub> in photocatalytic reactions. The precursors for g-C<sub>3</sub>N<sub>4</sub> can be mixed with the pre-formed TiO<sub>2</sub><sup>28,29,31</sup> or its precursors<sup>26,27,30</sup> to undergo calcination<sup>26–30</sup> or refluxing,<sup>31</sup> forming core-shell<sup>29,31</sup> or particles attached to sheets<sup>26–28</sup> structures with improved

<sup>a</sup> Department of Chemistry and <sup>c</sup> Department of Materials Science and Engineering, Southern University of Science and Technology, Shenzhen, 518055, China.

<sup>b</sup> Dalian Institute of Chemical Physics, Chinese Academy of Sciences, Dalian 116023, China.

† Footnotes relating to the title and/or authors should appear here.  
Electronic Supplementary Information (ESI) available: [the results of TGA and N<sub>2</sub> sorption measurements, SEM and low-magnified TEM images, and the stability test results]. See DOI: 10.1039/x0xx00000x

photocatalytic activity. As for the as-formed binary components, co-calcination has been frequently applied, resulting in particles on nanosheets g-C<sub>3</sub>N<sub>4</sub>/TiO<sub>2</sub> structures.<sup>32–34</sup> In addition, charge-induced aggregation has been proposed for constructing intimate heterojunctions of 0D/2D Nb<sub>2</sub>O<sub>5</sub>/g-C<sub>3</sub>N<sub>4</sub>,<sup>15</sup> 2D/2D g-C<sub>3</sub>N<sub>4</sub>/graphene oxide,<sup>36</sup> 2D/2D graphene/SnNb<sub>2</sub>O<sub>6</sub>,<sup>37</sup> etc. Among the various morphologies, 2D/2D heterojunction has unique merits compared with 0D/1D, 1D/1D, 0D/2D and 1D/2D interfaces, owing to the increased contact region and the intimate interface regardless of lattice mismatch, as well as the large lateral size with high surface area, to promote charge transfer and electron-hole separation, thereby improving the photocatalytic performance.<sup>19,24,25,36,37</sup> Meanwhile, the formation of 2D/2D heterostructure is also beneficial for the catalyst stability against photocorrosion and agglomeration.<sup>19,24,25,36,37</sup> However, relatively scarce works have been conducted concerning fabrication of 2D/2D heterostructure of TiO<sub>2</sub> and g-C<sub>3</sub>N<sub>4</sub>,<sup>24,25</sup> let alone comparing different construction approaches and clarifying the interfacial interaction modes.

Moreover, a third component has been frequently involved to form a ternary composite,<sup>38–42</sup> for example metallic Ag was incorporated to g-C<sub>3</sub>N<sub>4</sub>/TiO<sub>2</sub> to facilitate interfacial electron transfer,<sup>38</sup> Cu to MoO<sub>3</sub>/g-C<sub>3</sub>N<sub>4</sub> to boost visible light absorption for the surface plasmon resonance effect,<sup>39</sup> Al<sub>2</sub>O<sub>3</sub> to g-C<sub>3</sub>N<sub>4</sub>/ZnO to remedy the lattice mismatch,<sup>40</sup> etc. Nevertheless, the ternary nanocomposites bring in larger complexity than the binary nanocomposites, due to the more intricate interfaces.

Herein, we investigated differently fabricated TiO<sub>2</sub> and g-C<sub>3</sub>N<sub>4</sub> 2D/2D nanocomposites for efficient and stable photocatalytic H<sub>2</sub> evolution under visible-light irradiation. The preparation methods, *in-situ* solvothermal treatment, co-calcination and charge induced aggregation, were adopted with the aim of finely tuning the interfacial properties for the facilitation of electron-hole separation and electron transfer. By analyzing the photocatalytic performance and the physicochemical properties of each type of the composite, formation of interfacial covalent Ti-O-N bonds is more favorable than electrostatic interactions for promoting electron transfer and suppressing charge recombination. Meanwhile, large surface area of the composite needs to be ensured for abundant deposition of co-catalyst.

## Experimental

### Materials

Poly(ethylene oxide)-block-poly(propylene oxide)-block-poly(ethylene oxide) triblock copolymer (Pluronic P123, EO<sub>20</sub>PO<sub>70</sub>PEO<sub>20</sub>, M<sub>w</sub> = 5800) was purchased from Sigma-Aldrich (USA). Titanium isopropoxide (TTIP), hydrochloric acid, ethylene glycol, melamine, ethanol, sodium borohydride, H<sub>2</sub>PtCl<sub>6</sub> and triethanolamine (TEOA) were purchased from Aladdin Industrial Corporation (Shanghai, China). All reagents were used as-received without further purification.

### Synthesis of raw TiO<sub>2</sub> and g-C<sub>3</sub>N<sub>4</sub>

The ultrathin TiO<sub>2</sub> nanosheets were prepared using an solvothermal self-assembly method.<sup>24,43</sup> Namely, 200 mg of raw TiO<sub>2</sub> was ground thoroughly with 200 mg of NaBH<sub>4</sub> at room temperature. The mixture was transferred to a porcelain boat and heated in N<sub>2</sub> flow at 220 °C for 20 min with the ramp of 10 °C/min. The product was collected by washing with H<sub>2</sub>O to remove excessive NaBH<sub>4</sub> and drying at 60 °C overnight.

The modification of g-C<sub>3</sub>N<sub>4</sub> was performed by hydrothermal treatment<sup>45</sup> or acid treatment<sup>46</sup> to generate O-CN and H-CN, respectively. Briefly, for O-CN, 200 mg of g-C<sub>3</sub>N<sub>4</sub> was dispersed in 100 mL H<sub>2</sub>O by ultrasonication for 30 min and transferred to a 200 mL Teflon-lined autoclave for heating at 180 °C for 4 h. The solid sample was collected by centrifugation, washing with H<sub>2</sub>O and drying at 60 °C overnight. For H-CN, 500 mg of g-C<sub>3</sub>N<sub>4</sub> was mixed with 12.5 mL of concentrated HCl (37.5 wt.%) at room under stirring for 1 h. The solid sample was collected by centrifugation, washing with H<sub>2</sub>O to remove excessive HCl and drying at 60 °C overnight.

### Fabrication of three TiO<sub>2</sub> and g-C<sub>3</sub>N<sub>4</sub> nanocomposites

**Method I.** The bottom-up synthesis method of solvothermal *in-situ* growth of TiO<sub>2</sub> nanosheets on O-CN was used.<sup>24</sup> The protocol of precursor solution containing TTIP and P123 was the same with the synthesis of the raw TiO<sub>2</sub> nanosheets. 100 mg of O-CN was dispersed in 40 mL ethylene glycol by ultrasonication for 30 min. 5 mL of precursor solution was mixed with the above O-CN suspension and transferred to a 100 mL Teflon-lined autoclave for heating at 150 °C for 20 h. The yellow precipitates were extensively washed with ethanol and dried at 60 °C overnight to obtain the final product O-CN/TiO<sub>2</sub>.

**Method II.** Co-calcination of raw TiO<sub>2</sub> nanosheets with CN was applied, aiming at utilizing the thermal exfoliation of bulk g-C<sub>3</sub>N<sub>4</sub>.<sup>22,33,34,47</sup> 100 mg of raw TiO<sub>2</sub> and 100 mg of CN were added to 5 mL of ethanol and the resultant suspension was vigorously stirred at room temperature for 1 h and ultrasonicated for 20 min. The powder from drying the milky mixture at 60 °C overnight was placed in a covered porcelain boat for calcination in air at 450 °C for 2 h with the ramp of 10 °C/min. The targeted product was denoted as CN/TiO<sub>2</sub>-cal.

**Method III.** Charge-induced aggregation of H-TiO<sub>2</sub> and H-CN was performed to form intimate contact at the heterojunction with the driving force of electrostatic interaction. 100 mg of proton-functionalized g-C<sub>3</sub>N<sub>4</sub> (H-CN) whose zeta-potential is positive when dispersed in H<sub>2</sub>O,<sup>36</sup> and 100 mg of NaBH<sub>4</sub>-reduced TiO<sub>2</sub> nanosheets (H-TiO<sub>2</sub>) were dispersed in 100 mL H<sub>2</sub>O respectively under ultrasonication for 1 h. Then the two suspensions were mixed and ultrasonicated in ice bath for 2 h to achieve homogeneous suspension. Note that the pH changes were insignificant during the whole experiment and the final pH was still neutral. The material was centrifuged and dried at 60 °C overnight to yield the final product H-CN/H-TiO<sub>2</sub>. As a control, 100 mg of raw TiO<sub>2</sub> was ground manually with 100 mg of O-CN, and the resultant sample was denoted as "O-CN TiO<sub>2</sub> mixed".

### Characterizations

Zeta potentials were obtained by dynamic light-scattering analysis using the Zetasizer Nano ZS90 analyzer. 20 mg of each sample was dispersed in 50 mL of H<sub>2</sub>O by ultrasonication for the Zeta potential analysis. Thermogravimetric (TGA) measurements were performed in a Mettler-Toledo TGA instrument. About 10 mg of each sample was placed in an alumina crucible and heated to 800 °C at a heating rate of 10 °C/min in an air flow. X-ray diffraction (XRD) patterns were acquired on a Rigaku Smartlab-9kW X-ray diffractometer at 2θ from 5 to 80° and a scan speed of 5 °/min. Fourier transform infrared spectra (FTIR) were recorded on a Bruker IFS 66 spectrometer with 128 scans at a resolution of 2 cm<sup>-1</sup>. The samples were finely ground with KBr for the transparent pellets. Specific surface area and pore structure of each sample were determined by nitrogen sorption analysis using Micromeritics ASAP 2020. Scanning electron microscopy (SEM) images were obtained on a Tescan MIRA3 scanning electron microscope. Transmission electron microscopy (TEM) images were acquired on a JEM-2100 electron microscope operating at 200 kV. The samples for TEM were prepared by depositing an ethanolic suspension of each sample onto holey carbon coated copper grids and drying. The electron microscopy data (EDS, HAADF STEM) were acquired using the Cs aberration-corrected FEI Titan Themis G2 at 200 kV equipped with an ultra-high brightness gun and super-X EDS detector. X-ray photoelectron spectroscopy (XPS) measurement was carried out with Thermo SCIENTIFIC ESCALAB 250Xi instrument using a monochromatized Al Kα as the excitation source. C 1s signal at 284.8 eV was used to calibrate the binding energy (BE) and Shirley-type background was applied for each spectrum. UV-vis diffuse reflectance spectra (UV-vis DRS) of the samples were recorded using Lambda 950 UV/Vis/NIR spectrometer (Perkin Elmer) equipped with a diffuse reflectance attachment of a spectralon-coated integrating sphere against BaSO<sub>4</sub> reference. Photoluminescence (PL) spectra were collected on a fluorescence spectrometer (Horiba PTI QuantaMaster 400) at room temperature with a laser excitation wavelength of 330 nm.

### Photocatalytic testing

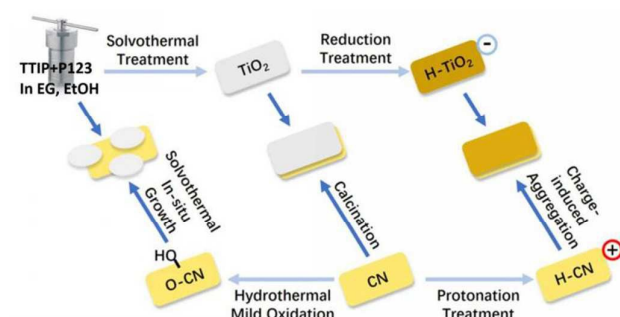
The photocatalytic hydrogen evolution reactions were performed using an online photocatalytic hydrogen generation system (CEL-SPH2N, AuLight, Beijing). A 300 W Xe lamp (CEL-HX300) equipped with a UV cut-off filter (UVIRCUT400, AuLight, Beijing, λ > 400 nm) was used as the visible light source, which was fan-cooled during the experiment. To maintain the ambient temperature of reaction system under irradiation, a liquid trap system with water circulation was used. In a typical test, 50 mg of photocatalyst was dispersed in 50 mL of aqueous solution containing 20 vol.% of TEOA as sacrificial reagent. 3 wt.% of Pt co-catalyst was photo-deposited uniformly on surface of photocatalyst using H<sub>2</sub>PtCl<sub>6</sub> as precursor. Before irradiation, the suspension was degassed thoroughly by evacuation to remove dissolved gases. After an adequate photo-depositing period, the gaseous product was analyzed every hour. H<sub>2</sub> evolution was quantitatively determined by an online gas chromatography (GC-7890,

thermal conductivity detector, molecular sieve 5 Å, N<sub>2</sub> carrier, Yiyou, Shanghai).

## Results and discussion

### Structural Characterizations of catalysts

Scheme 1 illustrates the three composite samples (O-CN/TiO<sub>2</sub>, CN/TiO<sub>2</sub>-cal and H-CN/H-TiO<sub>2</sub>) and their precursors (TiO<sub>2</sub>, TiO<sub>2</sub>-cal, H-TiO<sub>2</sub>, CN, O-CN and H-CN) investigated in this article. Solvothermal *in-situ* growth fabrication approach was detailed in our previous work.<sup>24</sup> Ultrathin TiO<sub>2</sub> nanosheets are formed *in-situ* by P123 template-assisted self-assembly and are attached to the edges of O-CN where oxygenated groups exist via Ti-O-N covalent linkages.<sup>24</sup> The as-formed Ti-O-N bonds under solvothermal treatment have been demonstrated to facilitate the efficient charge separation at interfaces and enhance the photocatalytic H<sub>2</sub> evolution activity. However, this composite still has residual P123 which may interfere with charge and mass transfer in the photocatalytic process.<sup>25</sup> Besides, other interaction modes of the interface of TiO<sub>2</sub> and g-C<sub>3</sub>N<sub>4</sub> for instance electrostatic Coulombic force and the influence of exfoliation degree of g-C<sub>3</sub>N<sub>4</sub> remain to be explored. Therefore, two distinct and versatile approaches, *i.e.* co-calcination and charge-induced self-assembly were also applied, to further investigate the contribution of the architecture of interface to the photocatalytic hydrogen evolution reaction. During co-calcination, the thermal exfoliation of g-C<sub>3</sub>N<sub>4</sub>,<sup>22,33,34,47</sup> the removal of P123 organic residue<sup>25,48</sup> and the increased crystallinity<sup>25,48</sup> are expected, which could be beneficial for the formation of close 2D/2D interfacial contact. During surface charge-induced aggregation, the oppositely-charged nanosheets could result in improved interaction between TiO<sub>2</sub> and g-C<sub>3</sub>N<sub>4</sub>, and thus the charge transfer across the heterojunction to promote the photocatalytic activity.<sup>15,36,37</sup>



**Scheme 1.** Schematic illustration of the three synthesis approaches of forming three composite samples (O-CN/TiO<sub>2</sub>, CN/TiO<sub>2</sub>-cal and H-CN/H-TiO<sub>2</sub>).

TGA/DTG curves of the three composite samples (O-CN/TiO<sub>2</sub>, CN/TiO<sub>2</sub>-cal and H-CN/H-TiO<sub>2</sub>), the physically mixed sample (O-CN/TiO<sub>2</sub> mixed) and the precursors (TiO<sub>2</sub>, H-TiO<sub>2</sub>, CN, O-CN and H-CN) are shown in Figure S1. For the nanocomposites, aside from the H<sub>2</sub>O desorption peak below 200 °C, the sharp DTG



peak at about 300 °C is assigned to the P123 residues,<sup>24,25,48</sup> and the peak starting from about 450 °C is due to the burn-off of g-C<sub>3</sub>N<sub>4</sub> species. The weight losses at different temperature stages are summarized in Table 1. The similar weight percentages of g-C<sub>3</sub>N<sub>4</sub> species for the three nanocomposites and the simple physical mixture rationalize the comparison of the physicochemical properties among these materials. The amount ratio of g-C<sub>3</sub>N<sub>4</sub> to TiO<sub>2</sub> is roughly 1:1 in all the composites in this work; 1:1 ratio has been found as the optimized value for construction of heterojunction in O-CN/TiO<sub>2</sub> samples (g-C<sub>3</sub>N<sub>4</sub> to TiO<sub>2</sub> ratio of 1:1, 1:2 and 2:1 were investigated.) without compromising the large surface area.<sup>24</sup> It is also noteworthy that the content for P123 residuals decreases to zero, following the order of O-CN/TiO<sub>2</sub>, H-CN/H-TiO<sub>2</sub> and CN/TiO<sub>2</sub>-cal.

Table 1 also lists the textural properties of the composites and the precursors. The N<sub>2</sub> sorption isotherms and pore size distributions are plotted in Figure S2. All the materials present type IV isotherms with H4 type hysteresis loops, which are caused by the stacking of nanosheets forming slit-like pores. The raw TiO<sub>2</sub> shows a large surface area of 330 m<sup>2</sup> g<sup>-1</sup>, while pristine CN shows S<sub>BET</sub> of only 12 m<sup>2</sup> g<sup>-1</sup>. The average pore size of CN is much larger than TiO<sub>2</sub>. These results indicate that the solvothermally synthesized TiO<sub>2</sub> is highly exfoliated and of relatively small sheet size, while CN is largely bulky. The O-CN and H-CN increase the surface area to 55 and 19 m<sup>2</sup> g<sup>-1</sup> respectively, proving the delamination effect during these treatments.<sup>45,46</sup> After formation of heterojunctions with TiO<sub>2</sub> in the three distinct ways, the surface areas increase tremendously to 73, 263 and 163 m<sup>2</sup> g<sup>-1</sup> for CN/TiO<sub>2</sub>-cal, O-CN/TiO<sub>2</sub> and H-CN/H-TiO<sub>2</sub>, respectively. The surface area of the composite is mainly contributed by TiO<sub>2</sub> component. The high surface area of O-CN/TiO<sub>2</sub> implies the successful formation of ultrathin TiO<sub>2</sub> nanosheets under solvothermal conditions in the presence of O-CN. The high surface area would supply more photocatalytic reactive centers to speed up the hydrogen evolution reaction. Besides, CN/TiO<sub>2</sub>-cal possesses merely mesopores (V<sub>meso</sub> = 0.30 cm<sup>3</sup> g<sup>-1</sup>), whereas H-CN/H-TiO<sub>2</sub> show V<sub>micro</sub> of 0.04 cm<sup>3</sup> g<sup>-1</sup> out of V<sub>tot</sub> of 0.17 cm<sup>3</sup> g<sup>-1</sup>. These results suggest the different origins of the slit-like pores. It is likely that the mesopores in CN/TiO<sub>2</sub>-cal are from the vacancy after the removal of P123 residuals and the stacking of the nanosheets. As for H-CN/H-TiO<sub>2</sub>, compact stacking driven by electrostatic Coulombic force can be envisaged, resulting in relatively high microporosity. Moreover, it has been found that very small pores around 2.14 nm in porous g-C<sub>3</sub>N<sub>4</sub> from kaolinite-templated synthesis still endowed reactive surface area for photocatalytic hydrogen evolution with Pt as co-catalyst.<sup>49</sup> Therefore, there may be no diffusion limitation in micropores and the surface area could serve as an evaluation criterion for the amount of photocatalytic reactive centers.

**Table 1. Compositional and textural properties of the TiO<sub>2</sub> and g-C<sub>3</sub>N<sub>4</sub> nanocomposites and their precursors.**

Entry	Catalyst	TiO <sub>2</sub> <sup>a</sup> (wt.%)	g-C <sub>3</sub> N <sub>4</sub> species	P123 residuals <sup>c</sup> (wt.%)	S <sub>BET</sub> <sup>d</sup> (m <sup>2</sup> g <sup>-1</sup> )	V <sub>tot</sub> <sup>e</sup> (cm <sup>3</sup> g <sup>-1</sup> )	V <sub>meso</sub> <sup>f</sup> (cm <sup>3</sup> g <sup>-1</sup> )	Average pore size <sup>g</sup> (nm)
-------	----------	---	--	--	--	---	--	---

1	TiO <sub>2</sub>	59	-	13	330	0.41	0.36	5.0
2	H-TiO <sub>2</sub>	68	-	10	n.d.	n.d.	n.d.	n.d.
3	CN	0	99	-	12	0.12	0.12	43.5
4	O-CN	0	98	-	55	0.20	0.20	14.7
5	H-CN	0	90	-	19	0.12	0.12	25.8
6	CN/TiO <sub>2</sub> -cal	57	45	0	73	0.30	0.30	16.3
7	O-CN/TiO <sub>2</sub>	37	47	8	263	0.57	0.53	8.7
8	H-CN/H-TiO <sub>2</sub>	37	50	5	163	0.17	0.13	4.3
9	O-CN TiO <sub>2</sub> mixed	35	48	8	n.d.	n.d.	n.d.	n.d.

a Weight percentage of TiO<sub>2</sub> was determined from the plateau in the high temperature range of TGA curves for samples containing TiO<sub>2</sub>.

b Weight percentage of residual P123 was determined from the weight loss around 300 °C of the TGA curves for samples containing TiO<sub>2</sub>.

c Weight percentage of g-C<sub>3</sub>N<sub>4</sub> species was determined from the main weight loss above 450 °C of the TGA curves for samples containing g-C<sub>3</sub>N<sub>4</sub>.

d Surface area (S<sub>BET</sub>) was calculated from the N<sub>2</sub> sorption isotherms by the Brunauer-Emmett-Teller (BET) method.

e Total pore volume (V<sub>pore</sub>) was calculated from the saturation plateau at high relative pressures.

f Mesopore volume (V<sub>meso</sub>) was calculated by subtracting micropore volume from V<sub>pore</sub>-the t-plot method.

g Pore size (D<sub>pore</sub>) was calculated from the adsorption branch of the isotherms by the Barrett-Joyner-Halenda (BJH) method.

XRD patterns of the TiO<sub>2</sub> and g-C<sub>3</sub>N<sub>4</sub> composites and precursors are shown in Figure 1. The characteristic peaks corresponding to (101), (004), (200), (105), (211) and (204) planes of anatase are identified with the XRD database. These diffraction peaks are obvious with TiO<sub>2</sub>-cal and CN/TiO<sub>2</sub>-cal, whereas the raw TiO<sub>2</sub> sheets, O-CN/TiO<sub>2</sub> and H-CN/H-TiO<sub>2</sub> are largely amorphous in TiO<sub>2</sub> phase with minor rutile phase as well. Calcination at 450 °C improves the crystallization degree of TiO<sub>2</sub> nanosheets and transformed them to pure anatase phase, consistence with the reported observation.<sup>48</sup> In the co-calcined CN/TiO<sub>2</sub>-cal, TiO<sub>2</sub> nanosheets also grow into anatase phase in the presence of CN. For g-C<sub>3</sub>N<sub>4</sub> precursors and the composite samples, the peaks corresponding to (100) and (200) planes of g-C<sub>3</sub>N<sub>4</sub> are observed, attributed to the in-plane repeated tri-s-triazine units and stacking of the conjugated N-containing aromatic ring, respectively.<sup>41</sup> The crystallinity of O-CN is more or less the same to CN, while H-CN is less ordered than CN, in terms of the peak intensity of CN(200). The CN(200) for the three composites remain at the same position compared to the g-C<sub>3</sub>N<sub>4</sub> precursors and the peak widths are in the objective order of crystallinity of the g-C<sub>3</sub>N<sub>4</sub> part, indicating that presence of TiO<sub>2</sub> did not influence the crystal structure of g-C<sub>3</sub>N<sub>4</sub>. The XRD pattern of the composite sample can be treated as supposition of individual TiO<sub>2</sub> and g-C<sub>3</sub>N<sub>4</sub> precursors.

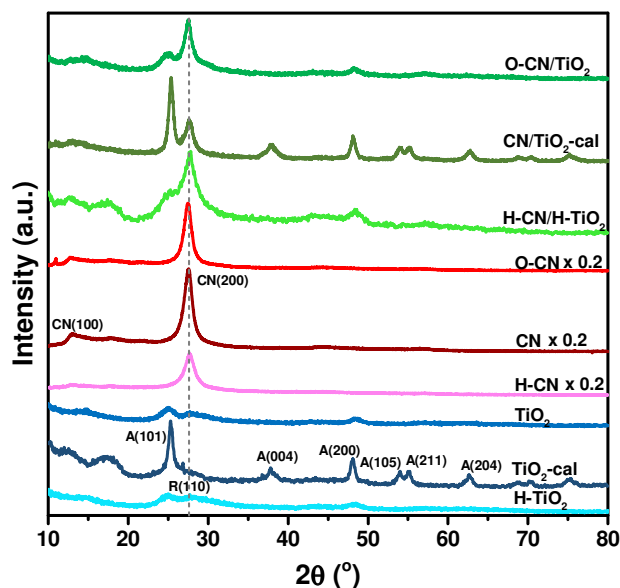


**Figure 1.** XRD patterns of the three composite samples (O-CN/TiO<sub>2</sub>, CN/TiO<sub>2</sub>-cal and H-CN/H-TiO<sub>2</sub>) and the precursors (TiO<sub>2</sub>, TiO<sub>2</sub>-cal, H-TiO<sub>2</sub>, CN, O-CN and H-CN). The A, R and CN are representing anatase, rutile and g-C<sub>3</sub>N<sub>4</sub>, respectively.

The FTIR spectra are presented in Figure 2. For the pristine TiO<sub>2</sub> nanosheets, the absorption peak around 1635 cm<sup>-1</sup> is attributed to O-H bending vibration.<sup>38</sup> The two small peaks at 2935 and 2868 cm<sup>-1</sup> are attributed to C-H stretching vibrations of the residue P123 species. These organics also show the C-O stretching vibrations and C-H bending vibrations signals in the range of 1200-600 cm<sup>-1</sup>. The hydrogenated TiO<sub>2</sub> show lower intensity for P123 and these absorption bands disappear for the calcined TiO<sub>2</sub>, in line with the TGA results. For g-C<sub>3</sub>N<sub>4</sub> precursors (CN, O-CN and H-CN), the characteristic absorption peaks are in similar shapes at the same positions. The strong bands in 1650-1200 cm<sup>-1</sup> are assigned to the typical stretching modes of tri-s-triazine skeleton ring and the peak at about 800 cm<sup>-1</sup> to the breathing mode of the triazine units.<sup>45,50</sup> The FTIR spectra of the three composites embody both characteristic absorption bands of the individual TiO<sub>2</sub> and g-C<sub>3</sub>N<sub>4</sub> precursors, indicating the coupling of TiO<sub>2</sub> with g-C<sub>3</sub>N<sub>4</sub> for each composite.

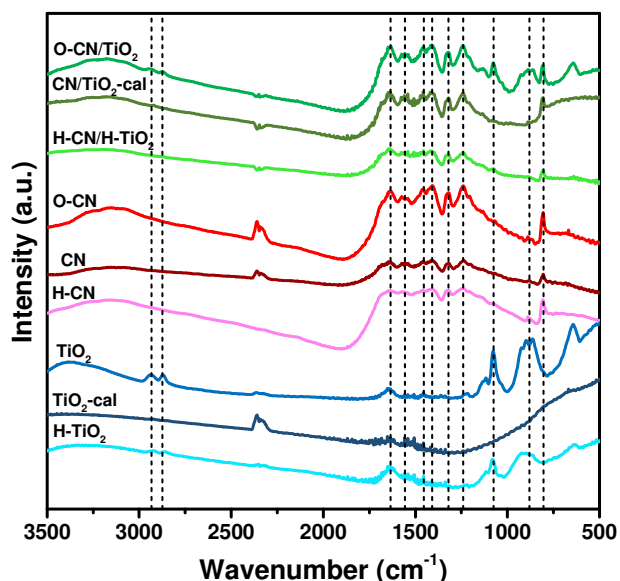


**Figure 2.** FTIR spectra of the three composite samples (O-CN/TiO<sub>2</sub>, CN/TiO<sub>2</sub>-cal and H-CN/H-TiO<sub>2</sub>) and the precursors (TiO<sub>2</sub>, TiO<sub>2</sub>-cal, H-TiO<sub>2</sub>, CN, O-CN and H-CN).

The morphology and microstructure of the three nanocomposites and the precursors were studied by TEM, as shown in Figure 3. The CN, O-CN and H-CN appears as relatively large and amorphous laminar morphologies, as reported elsewhere.<sup>24,36,46,50</sup> The protonated H-CN and the mildly-oxygenated O-CN show more exfoliated and less integrated sheets than the pristine CN.<sup>24,36,46</sup> The raw TiO<sub>2</sub> show poorly crystallized nanosheets with the thickness of *ca.* 1 nm and lengths of *ca.* 80 nm, consistent with previous report.<sup>43</sup> The calcination at 450 °C preserves the lamellar structure of TiO<sub>2</sub> sheets; the clear lattice fringe in the magnified region demonstrates the high degree of crystallization. The lattice distances of *ca.* 0.35 nm points to the (101) planes of anatase, in line with the XRD results. Hydrogenated H-TiO<sub>2</sub> show the crystallinity in-between raw TiO<sub>2</sub> and TiO<sub>2</sub>-cal, also with the presence of anatase phase. To be noted, the TiO<sub>2</sub> nanosheets in H-TiO<sub>2</sub> is more corrugated, perhaps due the mutual electrostatic repulsive force between the negatively charged sites in H-TiO<sub>2</sub>.<sup>36</sup> The TEM images of the three composites do not clearly show the interface of TiO<sub>2</sub> and g-C<sub>3</sub>N<sub>4</sub>, but the facts that the lattice fringes belongs to anatase TiO<sub>2</sub> and the size of g-C<sub>3</sub>N<sub>4</sub> sheets are relatively large help to distinguish TiO<sub>2</sub> from g-C<sub>3</sub>N<sub>4</sub> phases. The crystallinity of O-CN/TiO<sub>2</sub>, H-CN/H-TiO<sub>2</sub> and CN/TiO<sub>2</sub>-cal roughly follows the order of the corresponding pure TiO<sub>2</sub>, as revealed by XRD. All the three nanocomposites show the intertwined TiO<sub>2</sub> and g-C<sub>3</sub>N<sub>4</sub> regions under HRTEM, proving the close linkages and the compacted interfaces for the three distinct fabrication ways.

## Journal Name

## ARTICLE

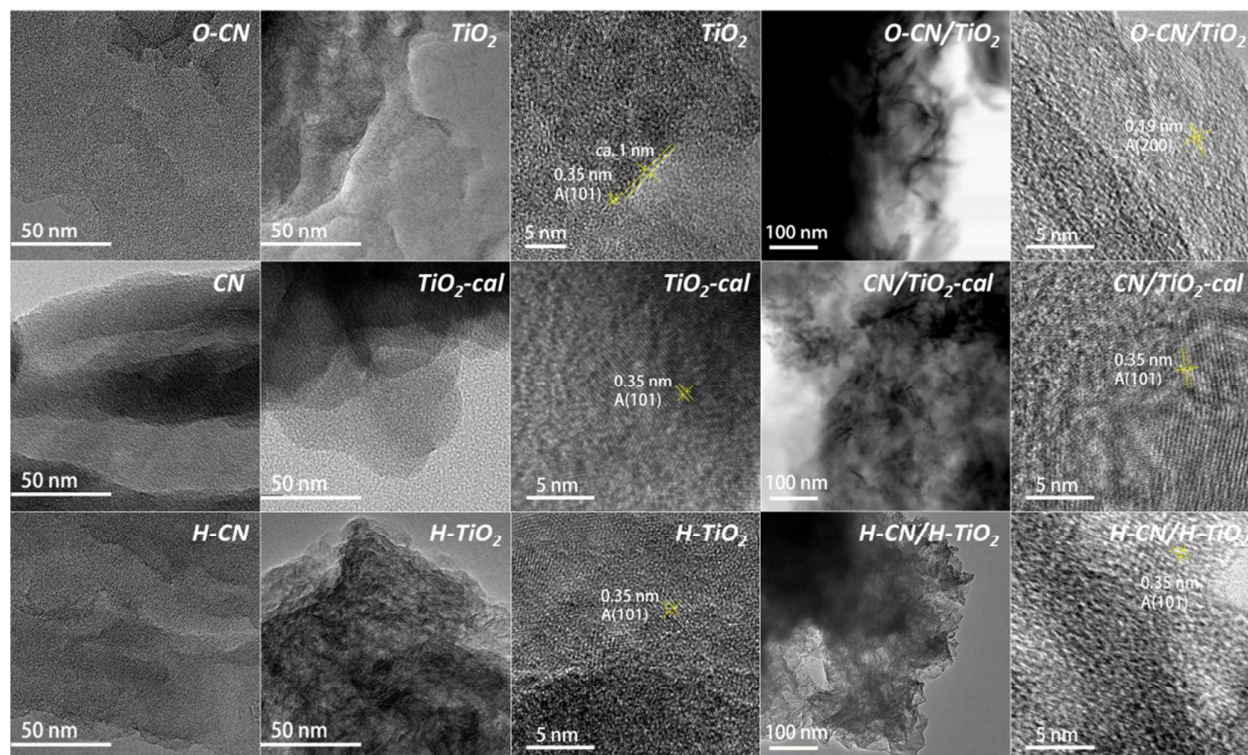


**Figure 3.** TEM images of the three composite samples (O-CN/TiO<sub>2</sub>, CN/TiO<sub>2</sub>-cal and H-CN/H-TiO<sub>2</sub>) and the precursors (TiO<sub>2</sub>, TiO<sub>2</sub>-cal, H-TiO<sub>2</sub>, CN, O-CN and H-CN).

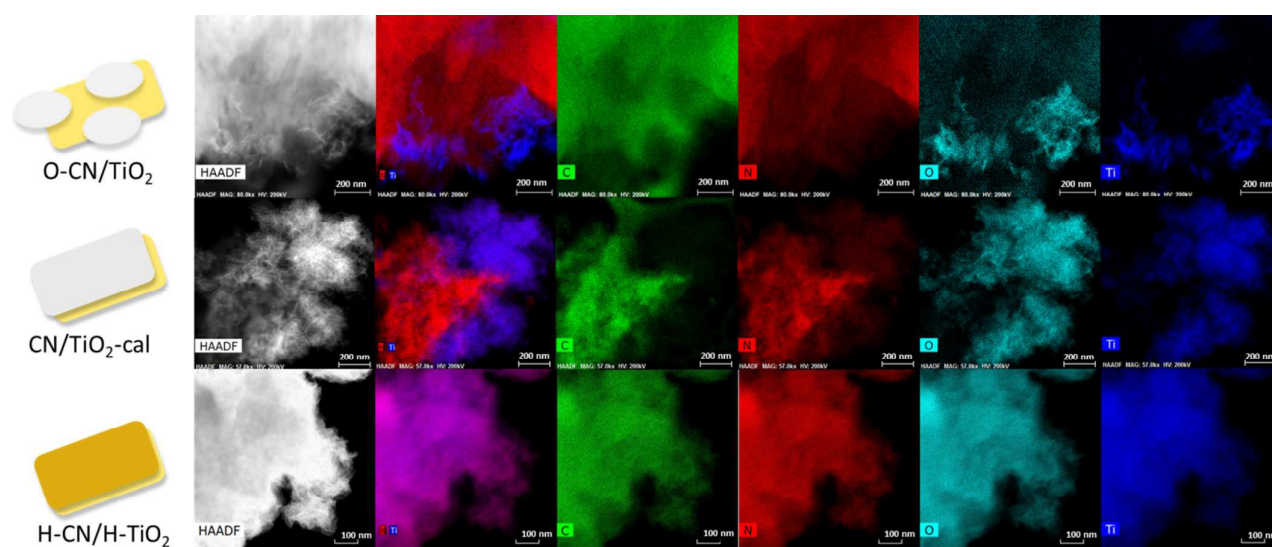


**Figure 4.** HAADF STEM images and EDS elemental mapping of C, N, O and Ti of the three nanocomposites (O-CN/TiO<sub>2</sub>, CN/TiO<sub>2</sub>-cal and H-CN/H-TiO<sub>2</sub>).



## Journal Name

## ARTICLE

The morphology and microstructure of the three nanocomposites and the precursors were studied by TEM, as shown in Figure 3. The CN, O-CN and H-CN appears as relatively large and amorphous laminar morphologies, as reported elsewhere.<sup>24,36,46,50</sup> The protonated H-CN and the mildly-oxygenated O-CN show more exfoliated and less integrated sheets than the pristine CN.<sup>24,36,46</sup> The raw TiO<sub>2</sub> show poorly crystallized nanosheets with the thickness of *ca.* 1 nm and lengths of *ca.* 80 nm, consistent with previous report.<sup>43</sup> The calcination at 450 °C preserves the lamellar structure of TiO<sub>2</sub> sheets; the clear lattice fringe in the magnified region demonstrates the high degree of crystallization. The lattice distances of *ca.* 0.35 nm points to the (101) planes of anatase, in line with the XRD results. Hydrogenated H-TiO<sub>2</sub> show the crystallinity in-between raw TiO<sub>2</sub> and TiO<sub>2</sub>-cal, also with the presence of anatase phase. To be noted, the TiO<sub>2</sub> nanosheets in H-TiO<sub>2</sub> is more corrugated, perhaps due the mutual electrostatic repulsive force between the negatively charged sites in H-TiO<sub>2</sub>.<sup>36</sup> The TEM images of the three composites do not clearly show the interface of TiO<sub>2</sub> and g-C<sub>3</sub>N<sub>4</sub>, but the facts that the lattice fringes belongs to anatase TiO<sub>2</sub> and the size of g-C<sub>3</sub>N<sub>4</sub> sheets are relatively large help to distinguish TiO<sub>2</sub> from g-C<sub>3</sub>N<sub>4</sub> phases. The SEM and low-magnified TEM images in Figure S3 both reflect that TiO<sub>2</sub> nanosheets were attached on large O-CN nanosheets in the nanocomposite of O-CN/TiO<sub>2</sub>. The crystallinity of O-CN/TiO<sub>2</sub>, H-CN/H-TiO<sub>2</sub> and CN/TiO<sub>2</sub>-cal roughly follows the order of the corresponding pure TiO<sub>2</sub>, as revealed by XRD. All the three nanocomposites show the intertwined TiO<sub>2</sub> and g-C<sub>3</sub>N<sub>4</sub> regions under HRTEM, proving close linkages and compacted interfaces for the three distinct fabrication ways.

The high-angle annular dark-field scanning TEM (HAADF-STEM) images and energy-dispersive X-ray spectroscopy (EDS) mappings are employed to ascertain the heterojunction structure and composition in the three nanocomposites, as shown in Figure 4. From the distributions of the four elements of C, N, O and Ti and their combined STEM image, O-CN/TiO<sub>2</sub> clearly shows many small ultrathin TiO<sub>2</sub> nanosheets bonded to the edges of large O-CN sheets, as observed before.<sup>24</sup> TiO<sub>2</sub> nanosheets are relatively individually standing on the O-CN sheets, due to the P123 templating effect during solvothermal *in-situ* growth synthesis. The interfacial Ti-O-N covalent bonds in O-CN/TiO<sub>2</sub> have been demonstrated by EDS point analysis.<sup>24</sup> In the co-calcined nanocomposite, though the TiO<sub>2</sub> phase is also in intimate contact with CN sheets, the self-aggregation of TiO<sub>2</sub> nanosheets is quite severe, which accounts from the removal of intercalating P123 residues. In case of H-CN/H-TiO<sub>2</sub>, the distributions of C, N, O and Ti are almost the same throughout the whole selected area. The 2D features of H-TiO<sub>2</sub>

and H-CN are well-preserved, and the charge-directed heteroaggregation upon ultrasonication results in effective formation of heterojunctions. The positively charged H-CN (with zeta potential equal to 5.5 mV in H<sub>2</sub>O) is likely to stack alternatively with the negatively charged H-TiO<sub>2</sub> (with zeta potential equal to -39.2 mV in H<sub>2</sub>O) into a layered 2D/2D heterostructure.

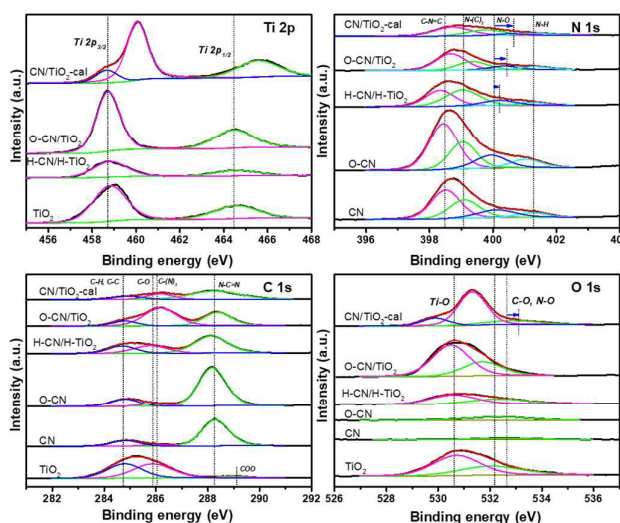


**Figure 5.** Ti 2p, N 1s, O 1s and C 1s XPS spectra of the three nanocomposites (O-CN/TiO<sub>2</sub>, CN/TiO<sub>2</sub>-cal and H-CN/H-TiO<sub>2</sub>) and the precursors (TiO<sub>2</sub>, CN and O-CN).

XPS was utilized to investigate the oxidation state and surface chemical compositions of the three TiO<sub>2</sub> and g-C<sub>3</sub>N<sub>4</sub> nanocomposites, bare TiO<sub>2</sub> and CNs, as shown in Figure 5. The C-H, C-C signals of C 1s from adventitious carbon were set to 284.8 eV for calibration. O-CN/TiO<sub>2</sub>, H-CN/H-TiO<sub>2</sub> and raw TiO<sub>2</sub> nanosheets all exhibit Ti 2p<sub>3/2</sub> and Ti 2p<sub>1/2</sub> with binding energies at 458.8 and 464.5 eV, respectively, ascribing to Ti<sup>4+</sup> species in the nanosheets with the presence of residual P123. The presence of Ti<sup>3+</sup> after NaBH<sub>4</sub> reduction hardly causes the alteration in the Ti 2p XPS spectra.<sup>44</sup> The peak positions are lower than the reference anatase (Ti 2p<sub>3/2</sub>=459.4 eV, Ti 2p<sub>1/2</sub>=465.3 eV) or rutile (Ti 2p<sub>3/2</sub>=459.3 eV, Ti 2p<sub>1/2</sub>=465.3 eV).<sup>43</sup> The CN/TiO<sub>2</sub>-cal shows a small component peak at 458.8 eV for Ti 2p<sub>3/2</sub>, while the main component peak is at 460.1 eV, 1.3 eV shift to the higher binding energy, indicating the formation of bulky TiO<sub>2</sub> species in the calcined sample.<sup>44,48</sup> The N 1s XPS spectrum shows four peaks at *ca.* 398.4, 399.0, 399.8 and 401.1 eV in bare CN, corresponding to N atoms in C-N=C, N-(C)<sub>3</sub>, N-O and N-H, respectively.<sup>24,29</sup> After hydrothermal



treatment, the N-O component increases in the N 1s peak, attributed to the introduction of oxygen. The acid treatment would not change the positions of the component peaks but lead to increase of N-H content.<sup>46</sup> After hybridization of g-C<sub>3</sub>N<sub>4</sub> with TiO<sub>2</sub>, the peak for N-O shifts toward high binding energy region to different degrees in the three nanocomposites, indicative of the bonding state of the heterojunction. O-CN/TiO<sub>2</sub> shows around 0.4 eV shift, indicating the formation of Ti-O-N covalent bonds, due to that the partial substitution of Ti-O-N with H-O-N and the resultant reduced electron density for the relatively electron-deficient Ti atoms. CN/TiO<sub>2</sub> show an even larger shift upward, *ca.* 0.5 eV, owing to the formation of Ti-O-N covalent bonds and the removal of P123 during the calcination procedure. On the contrary, H-CN/H-TiO<sub>2</sub>, shows only about 0.1 eV shift, in good accordance with the subtle change in the N 1s peak positions of 3CN:1Nb heterostructure which was prepared from the charge-induced aggregation of Nb<sub>2</sub>O<sub>5</sub> and g-C<sub>3</sub>N<sub>4</sub>.<sup>15</sup>

The C 1s spectra of CN are mainly composed of two peaks at 284.8 and 288.2 eV; the latter peak correspond to N-C=N in the triazine rings of g-C<sub>3</sub>N<sub>4</sub>.<sup>15,29</sup> The small peak at *ca.* 286.0 eV is assigned to C-(N)<sub>3</sub> species.<sup>29</sup> The C 1s spectrum of TiO<sub>2</sub> reflects the presence of P123 residues, which is slightly oxidized after the solvothermal synthesis. The nanocomposites of TiO<sub>2</sub> and g-C<sub>3</sub>N<sub>4</sub> show the peak at 288.2 eV featuring N-C=N of g-C<sub>3</sub>N<sub>4</sub>, and the peak at about 286.0 eV combining the C-(N)<sub>3</sub> groups of g-C<sub>3</sub>N<sub>4</sub> and C-O groups in P123 residues from TiO<sub>2</sub> part.

The O 1s peak in CN and O-CN locates at *ca.* 532.7 eV, arising from C-O or N-O groups in g-C<sub>3</sub>N<sub>4</sub>. O-CN shows higher amount of O than CN. As for TiO<sub>2</sub> nanosheets, O 1s peaks at 530.6 eV and 532.2 eV are identified, attributed to C-O from P123 residues and Ti-O respectively. O-CN/TiO<sub>2</sub> and H-CN/H-TiO<sub>2</sub> show similarly two peaks for O atoms. However, CN/TiO<sub>2</sub>-cal exhibits two peaks for Ti-O with a distance of 1.4 eV and an area ratio of 4.7 (close to 4.9, the area ratio of two peaks in Ti 2p). The blue shift of the main Ti-O peak is likely also due to the removal of P123 and the increased crystallinity. Meanwhile, the peak for O-C and O-N in CN/TiO<sub>2</sub>-cal shifts around 0.4 eV to high binding energy in relative to CN, possibly resulting from formation of Ti-O-N covalent bonds as a consequence of the relatively small electronegativity of Ti comparing with H. O-CN/TiO<sub>2</sub> should have such shifts as well, though overlapped by the O 1s signals from residual P123.

#### Photo spectral analysis and photocatalytic hydrogen evolution performance of catalysts

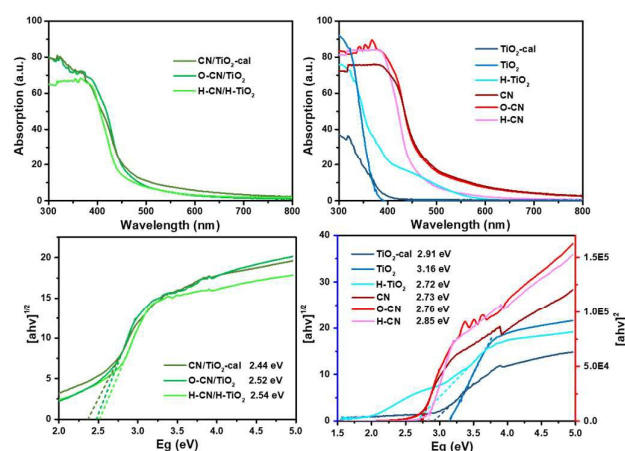


**Figure 6.** UV-vis DRS and the corresponding plots of  $(\alpha h\nu)^2$  or  $(\alpha h\nu)^{1/2}$  versus photon energy ( $h\nu$ ) of the three composite samples (O-CN/TiO<sub>2</sub>, CN/TiO<sub>2</sub>-cal and H-CN/H-TiO<sub>2</sub>) and the precursors (TiO<sub>2</sub>, TiO<sub>2</sub>-cal, H-TiO<sub>2</sub>, CN, O-CN and H-CN). The bandgap energies were indicated in the figure.

Figure 6 shows the UV-vis diffuse reflectance spectra (UV-vis DRS) of different TiO<sub>2</sub> and g-C<sub>3</sub>N<sub>4</sub> nanocomposites and their precursors. The raw TiO<sub>2</sub> and TiO<sub>2</sub>-cal have ultraviolet light absorptions almost below 400 nm, while the hydrogenated H-TiO<sub>2</sub> shows extended weak absorbance in 400-600 nm, characteristic of the reported black TiO<sub>2</sub> nanomaterials.<sup>7</sup> All g-C<sub>3</sub>N<sub>4</sub> samples have much greater absorbance in the visible light range of 400-600 nm. The post-treatment by mild oxidation in H<sub>2</sub>O does not influence much the absorbance, whereas the treatment by acid slightly blue-shifts the absorbance.<sup>45,46</sup> After combining TiO<sub>2</sub> with g-C<sub>3</sub>N<sub>4</sub> in three ways, the absorptions in both visible and ultraviolet light region are significantly enhanced. Compared to the individual precursors, the nanocomposites show the both characteristic light responses of TiO<sub>2</sub> and g-C<sub>3</sub>N<sub>4</sub>. The spectra of the three nanocomposites are close to each other, not a simple superposition of each precursor, which implies the synergistic effect between g-C<sub>3</sub>N<sub>4</sub> and TiO<sub>2</sub> to enhance the photoabsorption performance due to the construction of heterojunctions.

The band gap energy ( $E_g$ ) was calculated according to the plots transformed Kubelka-Munk (KM) function versus the light energy for the samples, as shown in Figure 6. The function is  $(\alpha h\nu)^2 = A(h\nu - E_g)$  or  $(\alpha h\nu)^{1/2} = A(h\nu - E_g)$  for direct or indirect transition semiconductor, respectively, where  $A$  is a constant,  $h\nu$  is photon energy,  $h$  is Planck's constant,  $\nu$  is the frequency of vibration, and  $\alpha$  is absorption coefficient.<sup>22,38</sup> The estimated band gap energy of TiO<sub>2</sub>-cal (2.91 eV) is smaller than raw TiO<sub>2</sub> nanosheets (3.16 eV), due to the increased crystallinity.<sup>48</sup> The hydrogenation of TiO<sub>2</sub> further narrowed the  $E_g$  to 2.72 eV, due to the increase of oxygen vacancies and Ti<sup>3+</sup> concentration.<sup>44</sup> The band gap energies of CN, O-CN and H-CN are 2.73, 2.76 and 2.85 respectively, consistent with the reported values.<sup>45,46</sup> The slight alternations are ascribed to the introduction of electron-withdrawing O groups and the quantum confinement effect, respectively.<sup>45,46</sup> The band gap energies for the

nanocomposites, O-CN/TiO<sub>2</sub>, CN/TiO<sub>2</sub>-cal and H-CN/H-TiO<sub>2</sub> are 2.44, 2.52 and 2.54 respectively, lower than the precursors of TiO<sub>2</sub> or g-C<sub>3</sub>N<sub>4</sub>. These results indicate that the photo-excitation occurs between the valence band (VB) of g-C<sub>3</sub>N<sub>4</sub> and the conduction band (CB) of TiO<sub>2</sub> part in these nanocomposites with efficient 2D/2D interfacial contact, ensuring the high light absorption efficiency and therefore the improved photocatalytic performance for H<sub>2</sub> evolution.

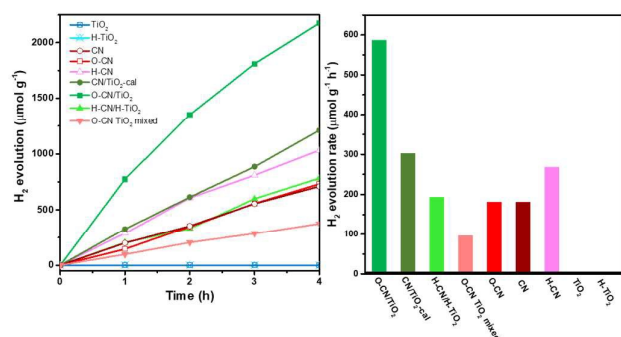


**Figure 7.** H<sub>2</sub> evolution of the three composite samples (O-CN/TiO<sub>2</sub>, CN/TiO<sub>2</sub>-cal and H-CN/H-TiO<sub>2</sub>), the physically mixed sample (O-CN TiO<sub>2</sub> mixed) and the precursors (TiO<sub>2</sub>, H-TiO<sub>2</sub>, CN, O-CN and H-CN) under visible light irradiation (left). The corresponding H<sub>2</sub> evolution rates (right).

The photocatalytic activity of the three TiO<sub>2</sub> and g-C<sub>3</sub>N<sub>4</sub> nanocomposites, the physically mixed sample and the precursors was assessed by photocatalytic hydrogen evolution under visible light irradiation ( $\lambda > 400$  nm) with 20 vol.% TEOA as sacrificial agent and 3 wt.% Pt as co-catalyst, as shown in Figure 7. The raw TiO<sub>2</sub> nanosheets show no photocatalytic activity due to the zero photo-absorption below 400 nm. The hydrogenated H-TiO<sub>2</sub> also show negligible H<sub>2</sub> evolution rate, perhaps due to the weak visible-light absorbance. For g-C<sub>3</sub>N<sub>4</sub> precursors, the time evolution curve for H<sub>2</sub> production of O-CN almost overlaps with CN, while the activity of H-CN is about 1.5 times that of CN in terms of the average H<sub>2</sub> evolution rate in the time span of 4 h. The reason could lie in the subtle modification of band structure in O-CN; the influence in the band structure after the introduction of oxygen to g-C<sub>3</sub>N<sub>4</sub> remains controversial in the literature.<sup>45,51,52</sup> The enhancement in the catalytic activity after acid treatment could be explained by the increased favorable defects, which expose more activity sites and decrease recombination sites.<sup>46</sup> The simple physical mixture of TiO<sub>2</sub> and g-C<sub>3</sub>N<sub>4</sub> would result in exactly half the H<sub>2</sub> evolution activity compared to the pure g-C<sub>3</sub>N<sub>4</sub>, as observed with O-CN TiO<sub>2</sub> mixed sample and O-CN. Weak Van der Waals interaction occurs in the "heterojunction" of the physical mixture, but does not accelerate the photocatalytic process. The hybridization with TiO<sub>2</sub> forming the three nanocomposites, however, significantly enhances the photocatalytic activity for H<sub>2</sub> evolution, in comparison with the physical mixture of the corresponding TiO<sub>2</sub> and g-C<sub>3</sub>N<sub>4</sub> precursors, indicating the synergic interaction between the two components across the interface. Among the three nanocomposites, O-CN/TiO<sub>2</sub> shows

the highest H<sub>2</sub> evolution rate, reaching a kinetic rate of 587  $\mu\text{mol g}^{-1} \text{h}^{-1}$ , which is about 6.1 times of the physical mixture. The photocatalytic activity stability of O-CN/TiO<sub>2</sub> nanocomposite was evaluated by extending the photo-irradiation time to 14 h. As shown in Figure S4, the average rate of H<sub>2</sub> formation is 566  $\mu\text{mol g}^{-1} \text{h}^{-1}$ , close to the average rate during the initial 4 h, indicating the maintenance of an excellent photocatalytic activity for H<sub>2</sub> evolution on O-CN/TiO<sub>2</sub>. The increase factors of the photocatalytic activity of CN/TiO<sub>2</sub>-cal and H-CN/H-TiO<sub>2</sub> are 3.4 and 1.4 times respectively, in relative to the physical mixture. Though the surface area of CN/TiO<sub>2</sub>-cal is the lowest among the three composites, the remarkable enhancement highlights the importance of forming covalent Ti-O-N bonds at the interface of TiO<sub>2</sub> and g-C<sub>3</sub>N<sub>4</sub> for the rapid charge carrier transfer and separation. The charge induced aggregated H-CN/H-TiO<sub>2</sub> sample, with a medium surface area and close 2D/2D face-to-face contact, does not avoid electron-hole recombination through electrostatic interaction as efficiently as through the covalent chemical bonds.

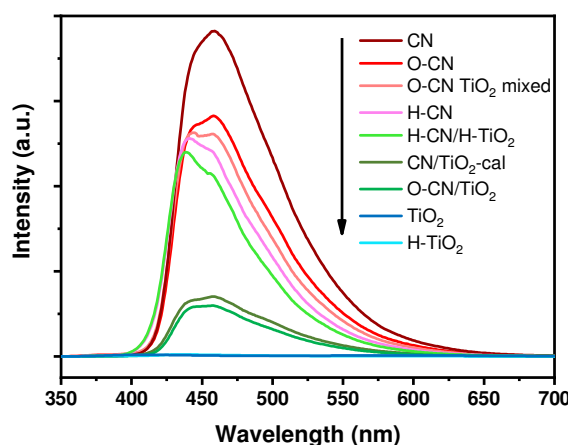


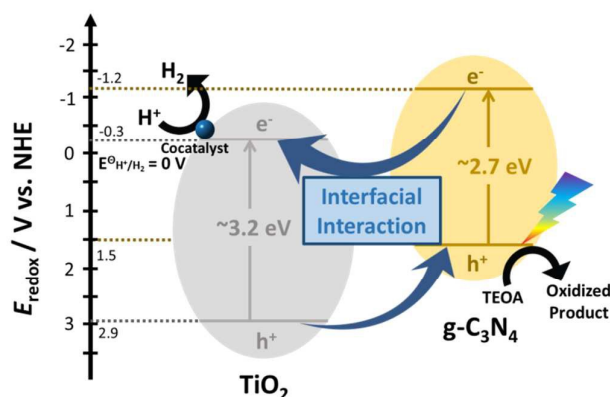
**Figure 8.** PL spectra of the three composite samples (O-CN/TiO<sub>2</sub>, CN/TiO<sub>2</sub>-cal and H-CN/H-TiO<sub>2</sub>), the physically mixed sample (O-CN TiO<sub>2</sub> mixed) and the precursors (TiO<sub>2</sub>, H-TiO<sub>2</sub>, CN, O-CN and H-CN) under 330 nm excitation.

PL spectra of the nanocomposite samples and the precursors are shown in Figure 8, revealing the recombination of charge carriers mainly in the g-C<sub>3</sub>N<sub>4</sub> part.<sup>29,34</sup> The highest PL emission intensity is observed with the pristine CN, indicating the most severe recombination of electron-hole pairs, as a result of n- $\pi^*$  electronic transitions involving lone pairs of N atoms.<sup>20,23</sup> The peak position locates at ca. 460 nm (*i.e.*, 2.7 eV), in conformity with the band gap energy derived from its UV-vis DRS spectrum.<sup>35</sup> The PL intensities decrease after the pretreatment of CN, consistent with previously reported results.<sup>45,46</sup> The formation of the three nanocomposites with TiO<sub>2</sub> further decreases the PL intensity, which is caused by the efficient separation of photogenerated electron-hole pairs between TiO<sub>2</sub> and g-C<sub>3</sub>N<sub>4</sub>.<sup>20,34,53</sup> The degree of PL quenching is in accordance with the photocatalytic hydrogen evolution results. The interfacial chemical bonds, *i.e.*, Ti-O-N, in O-CN/TiO<sub>2</sub> and

## ARTICLE

## Journal Name

CN/TiO<sub>2</sub>-cal most conspicuously facilitate the photogenerated charge separation and transfer, thereby effectively reducing the PL intensity and increasing the lifetime of photogenerated electrons and holes for the most prominently accelerated photocatalytic reactions. The recombination of photogenerated charge carriers is hardly inhibited in O-CN/TiO<sub>2</sub> mixed sample and slightly retarded in H-CN/H-TiO<sub>2</sub>, reflecting the dependence of PL intensity on the interaction modes between TiO<sub>2</sub> and g-C<sub>3</sub>N<sub>4</sub>, which also determine the photocatalytic performance.



**Scheme 2.** The energy diagram of the TiO<sub>2</sub> and g-C<sub>3</sub>N<sub>4</sub> composites for photocatalytic H<sub>2</sub> evolution under visible light irradiation.

The establishment of an intimate interfacial contact between TiO<sub>2</sub> nanosheets and g-C<sub>3</sub>N<sub>4</sub> is crucial to achieving high photocatalytic activity for H<sub>2</sub> evolution. Scheme 2 shows a tentative photocatalytic H<sub>2</sub> evolution mechanism catalyzed by TiO<sub>2</sub> and g-C<sub>3</sub>N<sub>4</sub> nanocomposites with deposited Pt under visible light irradiation. TiO<sub>2</sub> nanosheets have the VB and CB at about 2.9 and -0.3 eV (vs. NHE), respectively.<sup>30,34</sup> The calcination or hydrogenation by NaBH<sub>4</sub> do not turn TiO<sub>2</sub> into strong visible-light absorber. Calcination largely reduces the surface area though the crystallinity increases and P123 organic residues are removed. The VB and CB of CN locate at about 1.5 and -1.2 eV, respectively.<sup>16,30,46</sup> The mild oxidation or acid treatment results in slight modification of the band structure.<sup>46,52</sup> These treatments and calcination<sup>50</sup> indeed exfoliate CN, but still contribute a minor surface area in the nanocomposites with TiO<sub>2</sub>.

In the presence of the three TiO<sub>2</sub> and g-C<sub>3</sub>N<sub>4</sub> nanocomposites, at first, electrons in the VB of g-C<sub>3</sub>N<sub>4</sub> are excited to its CB under visible-light irradiation, forming the electron-hole pairs. The electrons in the CB of g-C<sub>3</sub>N<sub>4</sub> rapidly transfer to the CB of TiO<sub>2</sub> via the interfacial contact through either covalent Ti-O-N bonds (in O-CN/TiO<sub>2</sub> and CN/TiO<sub>2</sub>-cal) or the electrostatic Coulombic interaction (in H-CN/H-TiO<sub>2</sub>), realizing the efficient separation of photo-induced electrons and holes. The holes flowing from the VB of TiO<sub>2</sub> (2.9 eV) to the VB of g-C<sub>3</sub>N<sub>4</sub> (1.5 eV) are captured by TEOA. Simultaneously, the electrons flowing from the CB of g-C<sub>3</sub>N<sub>4</sub> (-1.2 eV) to the CB of TiO<sub>2</sub> (-0.3 eV) transfer to Pt for reduction of protons to H<sub>2</sub>. Pt co-catalyst easily sink the accumulated electrons, avoiding the excessive

accumulation and recombination of charge carriers.<sup>12,19,49</sup> Pt mainly deposits on the surface of TiO<sub>2</sub> due to the large surface area from its ultrathin 2D structure. Therefore, the facilitated electron-transfer across the g-C<sub>3</sub>N<sub>4</sub> and TiO<sub>2</sub> interface and the large surface area of TiO<sub>2</sub> phase are the two most important factors for improving the photocatalytic efficiency of H<sub>2</sub> evolution.

## Conclusions

In summary, three distinct and typical approaches were applied to fabricate TiO<sub>2</sub> and g-C<sub>3</sub>N<sub>4</sub> 2D/2D nanocomposites, *i.e.*, solvothermal treatment, co-calcination and surface charge-induced heteroaggregation. The resultant three heterostructures exhibits higher photocatalytic activities towards hydrogen evolution reaction under visible light irradiation, in comparison with the physical mixture of the corresponding g-C<sub>3</sub>N<sub>4</sub> and TiO<sub>2</sub> nanosheets, with an enhancement factor of 1.4-6.1. According to the analyses of the physicochemical properties, the formation of covalent Ti-O-N is evidenced to more efficiently facilitate the migration and separation of photoinduced charge carriers compared to electrostatic interactions, thus more beneficial for H<sub>2</sub> evolution. In addition, the maintenance of large surface area outweighs the surface-cleaness and crystallinity of TiO<sub>2</sub> component in the composites in terms of the photocatalytic H<sub>2</sub> evolution activity. The well-designed comparative experiments and detailed characterizations in this work may pave the way to rational design and synthesis of other composite materials with well-defined heterostructures for versatile applications.

## Conflicts of interest

There are no conflicts to declare.

## Acknowledgements

This work was financially supported by Southern University of Science and Technology start fund through Shenzhen Peacock Talent program, the basic research fund of Shenzhen (JCYJ20150507170334573), the technical research fund of Shenzhen (JSGG20160427105120572), and Guangdong Innovative and Entrepreneurial Research Team Program (No.2016ZT06N532). This work was also supported by the Pico Center at SUSTech that receives support from Presidential fund and Development and Reform Commission of Shenzhen Municipality.

## References

1. C. Acar, I. Dincer and G. F. Naterer, *Int. J. Energy Res.*, 2016, **40**, 1449-1473.
2. J. A. Turner, *Science*, 2004, **305**, 972-974.
3. P. Lianos, *Appl. Catal. B*, 2017, **210**, 235-254.



4. J. Schneider, M. Matsuoka, M. Takeuchi, J. Zhang, Y. Horiuchi, M. Anpo and D. W. Bahnemann, *Chem. Rev.*, 2014, **114**, 9919-9986.
5. S. Dong, J. Feng, M. Fan, Y. Pi, L. Hu, X. Han, M. Liu, J. Sun and J. Sun, *RSC Adv.*, 2015, **5**, 14610-14630.
6. A. Fujishima and K. Honda, *Nature*, 1972, **238**, 37-38.
7. S. G. Ullattil, S. B. Narendranath, S. C. Pillai and P. Periyat, *Chem. Eng. J.*, 2018, **343**, 708-736.
8. S. Chu, Y. Wang, Y. Guo, J. Feng, C. Wang, W. Luo, X. Fan and Z. Zou, *ACS Catal.*, 2013, **3**, 912-919.
9. W. Ong, L. Tan, Y. H. Ng, S. Yong and S. Chai, *Chem. Rev.*, 2016, **116**, 7159-7329.
10. J. Zhang, Y. Chen and X. Wang, *Energy Environ. Sci.*, 2015, **8**, 3092-3108.
11. Martha, S., Mansingh, S., Parida, K.M. and Thirumurugan, A., *Mater. Chem. Front.*, 2017, **1**, 1641-1653.
12. S. Patnaik, S. Martha and K. M. Parida, *RSC Adv.*, 2016, **6**, 46929-46951.
13. Patnaik, S., Martha, S., Acharya, S. and Parida, K.M., *Inorg. Chem. Front.*, 2016, **3**, 336-347.
14. S. Martha, A. Nashim and K. M. Parida, *J. Mater. Chem. A*, 2013, **1**, 7816-7824.
15. G. T. S. T. Da Silva, K. T. G. Carvalho, O. F. Lopes and C. Ribeiro, *Appl. Catal. B*, 2017, **216**, 70-79.
16. Q. Zhang, S. Yuan, B. Xu, Y. Xu, K. Cao, Z. Jin, C. Qiu, M. Zhang, C. Su and T. Ohno, *Catal. Today*, 2018, **315**, 184-193.
17. Y. Hong, Z. Fang, B. Yin, B. Luo, Y. Zhao, W. Shi and C. Li, *Int. J. Hydrogen Energy*, 2017, **42**, 6738-6745.
18. Y. Wang, Q. Wang, X. Zhan, F. Wang, M. Safdar and J. He, *Nanoscale*, 2013, **5**, 8326-8339.
19. T. Su, Q. Shao, Z. Qin, Z. Guo and Z. Wu, *ACS Catal.*, 2018, **8**, 2253-2276.
20. Z. Lu, L. Zeng, W. Song, Z. Qin, D. Zeng and C. Xie, *Appl. Catal. B*, 2017, **202**, 489-499.
21. K. Li, Z. Huang, X. Zeng, B. Huang, S. Gao and J. Lu, *ACS Appl. Mater. Interfaces*, 2017, **9**, 11577-11586.
22. F. Chang, J. Zhang, Y. Xie, J. Chen, C. Li, J. Wang, J. Luo, B. Deng and X. Hu, *Appl. Surf. Sci.*, 2014, **311**, 574-581.
23. J. Ma, X. Tan, F. Jiang and T. Yu, *Catal. Sci. Technol.*, 2017, **7**, 3275-3282.
24. R. Zhong, Z. Zhang, H. Yi, L. Zeng, C. Tang, L. Huang and M. Gu, *Appl. Catal. B*, 2018, **237**, 1130-1138.
25. W. Gu, F. Lu, C. Wang, S. Kuga, L. Wu, Y. Huang and M. Wu, *ACS Appl. Mater. Interfaces*, 2017, **9**, 28674-28684.
26. K. Li, S. Gao, Q. Wang, H. Xu, Z. Wang, B. Huang, Y. Dai and J. Lu, *ACS Appl. Mater. Interfaces*, 2015, **7**, 9023-9030.
27. S. Zhou, Y. Liu, J. Li, Y. Wang, G. Jiang, Z. Zhao, D. Wang, A. Duan, J. Liu and Y. Wei, *Appl. Catal. B*, 2014, **158-159**, 20-29.
28. N. Boonprakob, N. Wetchakun, S. Phanichphant, D. Waxler, P. Sherrell, A. Nattestad, J. Chen and B. Inceesungvorn, *J. Colloid Interface Sci.*, 2014, **417**, 402-409.
29. W. Wang, J. Fang, S. Shao, M. Lai and C. Lu, *Appl. Catal. B*, 2017, **217**, 57-64.
30. S. Pany and K. M. Parida, *Phys. Chem. Chem. Phys.*, 2015, **17**, 8070-8077.
31. Y. Wang, W. Yang, X. Chen, J. Wang and Y. Zhu, *Appl. Catal. B*, 2018, **220**, 337-347.
32. J. Li, M. Zhang, Q. Li and J. Yang, *Appl. Surf. Sci.*, 2017, **391**, 184-193.
33. J. Li, M. Zhang, X. Li, Q. Li and J. Yang, *Appl. Catal. B*, 2017, **212**, 106-114.
34. M. Reli, P. Huo, M. Šihor, N. Ambrožová, I. Troppová, L. Matějová, J. Lang, L. Svoboda, P. Kuřtrowski, M. Ritz, P. Praus and K. Kočí, *J. Phys. Chem. A*, 2016, **120**, 8564-8573.
35. Patnaik, S., Martha, S., Madras, G. and Parida, K.M., *Phys. Chem. Chem. Phys.*, 2016, **18**, 28502-28514.
36. W. Ong, L. Tan, S. Chai, S. Yong and A. R. Mohamed, *Nano Energy*, 2015, **13**, 757-770.
37. L. Yuan, M. Yang and Y. Xu, *Nanoscale*, 2014, **6**, 6335-6345.
38. Y. Chen, W. Huang, D. He, Y. Situ and H. Huang, *ACS Appl. Mater. Interfaces*, 2014, **6**, 14405-14414.
39. S. Patnaik, G. Swain and K. M. Parida, *Nanoscale*, 2018, **10**, 5950-5964.
40. S. Liu, F. Li, Y. Li, Y. Hao, X. Wang, B. Li and R. Liu, *Appl. Catal. B*, 2017, **212**, 115-128.
41. G. Jiang, K. Geng, Y. Wu, Y. Han and X. Shen, *Appl. Catal. B*, 2018, 366-375.
42. S. Patnaik, D. P. Sahoo, L. Mohapatra, S. Martha and K. M. Parida, *Energy Technol.*, 2017, **5**, 1687-1701.
43. Z. Sun, T. Liao, Y. Dou, S. M. Hwang, M. Park, L. Jiang, J. H. Kim and S. X. Dou, *Nature Commun.*, 2014, **5**, 3813-3821.
44. B. Yan, P. Zhou, Q. Xu, X. Zhou, D. Xu and J. Zhu, *RSC Adv.*, 2016, **6**, 6133-6137.
45. L. Ming, H. Yue, L. Xu and F. Chen, *J. Mater. Chem. A*, 2014, **2**, 19145-19149.
46. C. Dong, Z. Ma, R. Qie, X. Guo, C. Li, R. Wang, Y. Shi, B. Dai and X. Jia, *Appl. Catal. B*, 2017, **217**, 629-636.
47. J. Xu, Y. Chen, Y. Hong, H. Zheng, D. Ma, B. Xue and Y. Li, *Appl. Catal. A*, 2018, **549**, 31-39.
48. J. Yang, Y. Jiang, L. Li, E. Muhire and M. Gao, *Nanoscale*, 2016, **8**, 8170-8177.

## ARTICLE

Journal Name

49. Z. Zhang, L. Lu, Z. Lv, Y. Chen, H. Jin, S. Hou, L. Qiu, L. Duan, J. Liu and K. Dai, *Appl. Catal. B*, 2018, **232**, 384-390.
50. S. C. Yan, Z. S. Li and Z. G. Zou, *Langmuir*, 2009, **25**, 10397-10401.
51. Y. Huang, Y. Wang, Y. Bi, J. Jin, M. F. Ehsan, M. Fu and T. He, *RSC Adv.*, 2015, **5**, 33254-33261.
52. C. Wang, H. Fan, X. Ren, J. Ma, J. Fang and W. Wang, *ChemSusChem*, 2018, **11**, 700-708.
53. S. Nayak, L. Mohapatra and K. Parida, *J. Mater. Chem. A*, 2015, **3**, 18622-18635.